

Disentangling Core and Edge Mechanisms of the Density Limit in DIII-D Negative Triangularity Plasmas

R. Hong,¹ P.H. Diamond,² O. Sauter,³ J. Chen,¹ F. Khabanov,⁴ Z. Li,⁵
D. Liu,⁵ A. Marinoni,² G.R. McKee,⁴ T.L. Rhodes,¹ F. Scotti,⁶ K.E. Thome,⁵
G.R. Tynan,² M.A. Van Zeeland,⁵ Z. Yan,⁴ L. Zeng,¹ and the DIII-D NT Team

¹*University of California, Los Angeles, Los Angeles, California 90095, USA*

²*University of California, San Diego, La Jolla, California 92093, USA*

³*Ecole Polytechnique Fédérale de Lausanne (EPFL),
Swiss Plasma Center (SPC), Lausanne, Switzerland*

⁴*University of Wisconsin-Madison, Madison, Wisconsin 53706, USA*

⁵*General Atomics, San Diego, California, 92121, USA*

⁶*Lawrence Livermore National Laboratory, Livermore, California 94550, USA*

(Dated: July 2, 2025)

Abstract

The density limit is investigated in the DIII-D negative triangularity (NT) plasmas which lack a standard H-mode edge. We find the limit may not be a singular disruptive boundary but a multifaceted density saturation phenomenon governed by distinct core and edge transport mechanisms. Sustained, non-disruptive operation is achieved at densities up to 1.8 times the Greenwald limit (n_G) until the termination of auxiliary heating. Systematic power scans reveal distinct power scalings for the core ($n_e \propto P_{\text{SOL}}^{0.27 \pm 0.03}$) and edge ($n_e \propto P_{\text{SOL}}^{0.42 \pm 0.04}$) density limits. The edge density saturation is triggered abruptly by the onset of a non-disruptive, high-field side radiative instability that clamps the edge density below n_G . In contrast, the core density continues to rise until it saturates, a state characterized by substantially enhanced core turbulence. Core transport evolves from a diffusive to an intermittent, avalanche-like state, as indicated by heavy-tailed probability density functions (kurtosis ≈ 6), elevated Hurst exponents, and a $1/f$ -type power spectrum. These findings suggest that the density limit in the low-confinement regime is determined by a combination of edge radiative instabilities and core turbulent transport. This distinction provides separate targets for control strategies aimed at extending the operational space of future fusion devices.

I. INTRODUCTION

High plasma density is a fundamental requirement for achieving a self-sustaining fusion reaction, as fusion power scales strongly with density [1]. However, tokamak operation is constrained by an operational density limit [2–4]. Exceeding this critical density leads to a rapid loss of confinement, often culminating in a plasma termination. Overcoming this long-standing obstacle is therefore a critical step toward realizing economically viable fusion energy.

The conventional metric for the density limit is the empirical Greenwald scaling [2, 3]: n_G (10^{20} m^{-3}) = $\frac{I_p \text{ (MA)}}{\pi a^2 \text{ (m}^2\text{)}}$, where I_p denotes the plasma current and a the minor radius. This scaling is notably independent of heating power. This paradigm is increasingly challenged by observations that the achievable density scales favorably with heating power. Recent theoretical modeling [5, 6] and database analyses [7, 8] suggest that the achievable density limit in the low-confinement (L-mode) regime may increase with heating power, potentially exceeding the conventional Greenwald density. Furthermore, the power-dependent density limits have also been observed in stellarators [9, 10], which lack plasma current, suggesting a more uni-

versal physical basis rooted in power balance and transport that transcends specific magnetic configurations. Therefore, further dedicated investigations are needed to develop a physics-based understanding of the fundamental mechanisms governing density limits in magnetically confined plasmas.

The physics underpinning the L-mode density limit involves a complex interplay of several processes. Turbulent transport [11–15], radiative power losses [4, 7, 16], and magnetohydrodynamic (MHD) instabilities [17, 18] have all been reported as key contributors. These processes do not act in isolation; instead, they are coupled synergistically [3] and ultimately constrain the plasma density. Consequently, developing predictive models of density limits requires disentangling their individual roles and interdependencies.

To elucidate the fundamental physics of the L-mode density limit, it is advantageous to use a plasma configuration that approximates L-mode edge conditions over a wide range of operational parameters. This avoids the complexities introduced by the edge transport barriers (ETBs) and edge localized modes (ELMs), which are characteristic of conventional high-confinement (H-mode) plasmas. The negative triangularity (NT) plasmas [19, 20], characterized by an inverted “D”-shaped cross-section (see Fig. 1), provides an ideal platform for this study. These plasmas exhibit improved core confinement [21–24] while maintaining L-mode-like edge conditions. While the NT edge is not identical to that of a conventional positive triangularity L-mode, its lack of strong H-mode ETBs and ELMs makes it an excellent proxy for isolating the core and edge transport phenomena that govern density limits without confounding factors.

This paper presents an examination of the physics governing the density limit in NT plasmas on the DIII-D tokamak. We report the achievement of sustained, non-disruptive high-density operation, where the plasma density can surpass the conventional Greenwald density by a factor of 1.8 at substantial input power. A systematic power scan reveals disparate scaling dependencies for the core ($n_e \propto P_{\text{SOL}}^{0.27 \pm 0.03}$) and the separatrix ($n_e \propto P_{\text{SOL}}^{0.42 \pm 0.04}$) regions. Detailed experimental measurements reveal that different mechanisms determine density limits in the core and edge plasmas. At the plasma edge, the density is constrained by enhanced turbulence driven by a radiative instability. In contrast, the core density is not directly limited by the radiative cooling but eventually saturates due to the emergence of enhanced, avalanche-like turbulence. These findings challenge the traditional paradigm of a single disruptive limit, advancing a more nuanced picture where distinct processes govern density saturation in different plasma regions.

The remainder of this paper is structured as follows. Section II describes the experimental arrangement, including the plasma configuration and the diagnostic suite employed in this study. Section III presents our experimental findings, organized into four subsections: (1) high-density operation beyond the Greenwald density and the power dependence of the core and edge density limits; (2) the temporal evolution of equilibrium profiles and turbulence approaching the density limit; (3) the edge density limit and the role of radiative edge cooling; (4) the core density limit and the dominant role of avalanche-like turbulence. Finally, Section IV summarizes the key findings and discusses their broader implications for fusion research.

II. EXPERIMENTAL ARRANGEMENT

The experiment was conducted on the DIII-D tokamak [25], with auxiliary heating power provided by neutral beam injection (NBI) and varied between discharges. All discharges employed a lower single-null configuration with an open divertor geometry, and the ion $\mathbf{B} \times \nabla \mathbf{B}$ drift was directed away from the primary divertor, as illustrated in Fig. 1. The plasma shape was characterized by negative triangularity at both the top and bottom ($\delta_{\text{top}} = -0.3$ and $\delta_{\text{bot}} = -0.62$), moderate elongation ($\kappa \approx 1.3$), and an edge safety factor of $q_{95} = 4.1$. This paper focuses specifically on discharges with toroidal field $B_t = 2.0$ T and plasma current $I_p = 0.6$ MA. Additional experiments exploring different plasma current and toroidal field combinations are reported separately [26]. In each discharge, plasma density was gradually increased via gas puffing from the top of the mainchamber. Consistent with the behavior of NT plasmas, no edge localized modes were observed in any discharge.

A comprehensive suite of diagnostics monitored the evolving plasma state. Figure 1 shows the locations of the key diagnostics. Electron density and temperature in the main chamber were measured using the Thomson scattering (TS) system [27]. Charge exchange recombination (CER) spectroscopy [28] measured the temperature, density, and toroidal and poloidal rotation velocities of carbon ions. These impurity ion profiles were used to compute radial electric field profiles (E_r) using the carbon ion force balance equation. Bolometer arrays [29] provided measurements of the radiated power distribution and total radiated power.

Several diagnostics were used to probe density fluctuations. A multichannel CO₂ interferometer [30] measured the line-averaged density and its low- k fluctuations along one horizontal midplane chord and three vertical chords at major radii of $R = 1.48$ m (high-field

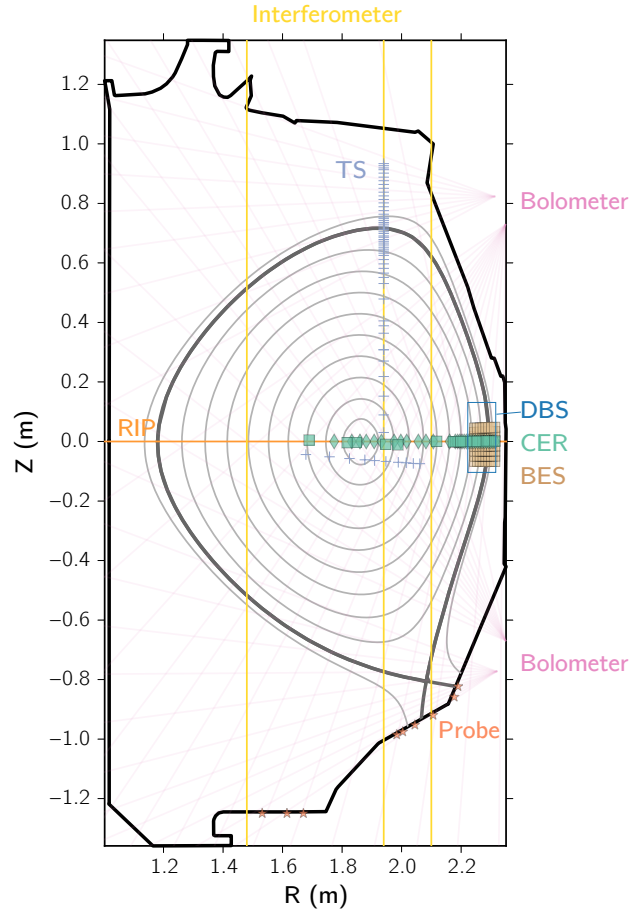


FIG. 1. Cross-section of DIII-D tokamak showing locations of key diagnostics used for the present study.

side), $R = 1.94$ m (core region), and $R = 2.10$ m (low-field side). The radial interferometer polarimeter (RIP) [31] also provided line-integrated measurements of electron density fluctuations at the mid-plane. A 2D array of high-sensitivity beam emission spectroscopy (BES) [32] measured ion-scale ($k_\theta < 3 \text{ cm}^{-1}$) density fluctuations at the edge. Two 8-channel Doppler back-scattering (DBS) systems [33, 34] measured turbulent flows and low-to-intermediate- k ($2 < k_\theta < 10 \text{ cm}^{-1}$) density fluctuations. The radial locations and corresponding wavenumbers of the DBS measurements were calculated using the 3D ray-tracing code GENRAY [35].

III. RESULTS

A. Achieving High Density Beyond the Greenwald Limit

1. Density Saturation Beyond the Greenwald Limit

A key result of this study is the achievement of sustained L-mode operation at densities that surpass the conventional Greenwald density limit. This is shown in Fig. 2, which presents the time evolution of key parameters in two representative discharges with different levels of auxiliary heating from NBI. Across the experiment, the NBI power was varied from 3 MW up to 13 MW. As shown in Figs. 2(b) and 2(c), both core and separatrix densities increase with input power. The core density at $\rho \approx 0.7$, which is similar to the line-averaged density, consistently exceeds the Greenwald density (n_G). Notably, rather than disrupting upon reaching their maximum density, the discharges with medium to high NBI power ($P_{\text{NBI}} > 4$ MW) transitioned into a phase of density saturation that persisted until the termination of auxiliary heating.

The radiated power in the divertor [Fig. 2(d)] and the main chamber [Fig. 2(e)] also increase with density, indicating enhanced radiative losses. The spikes in the divertor radiation power [Fig. 2(d)] mark the development of a radiation front that propagates from the divertor towards the high-field side (HFS).

The line-averaged density, inferred from Thomson scattering profiles, reached $1.8 \times n_G$ in the high-power discharge. For comparison, the CO₂ interferometer measured a line-averaged density of $2.0 \times n_G$ [20, 26]. This discrepancy arises because the interferometer's measurement includes the substantial scrape-off layer density present during high-density operation. Therefore, Thomson scattering measurements are used for the analysis in this study.

2. Disparate Power Scaling for Core and Edge Density Limit

Having established that the density limit in these NT plasmas is a saturation phenomenon, we investigate its dependence on heating power. The analysis correlates the maximum achieved density with the power flowing into the scrape-off layer (P_{SOL}), defined as $P_{\text{SOL}} = P_{\text{in}} - P_{\text{rad,core}} - dW/dt$, accounting for total input power, core radiated power, and changes in stored energy. This parameter represents the effective supplied heating. All values are averaged over a 100 ms window at the point of maximum density.

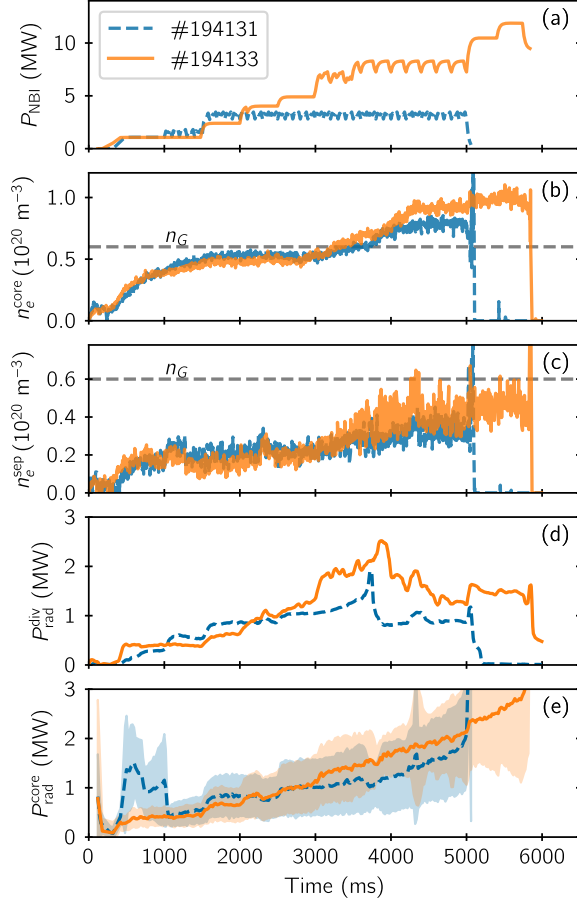


FIG. 2. Time history of relevant plasma parameters in two representative NT discharges with different power input levels. (a) NBI power input, (b) core density ($\rho = 0.7$), (c) separatrix density, (d) the radiated power in the divertor, and (e) radiated power in the core or mainchamber. The dashed horizontal line in (b) and (c) indicates the Greenwald density.

A systematic power scan reveals that the core and edge densities respond differently to P_{SOL} , as shown in Fig. 3. The maximum core density (at $\rho = 0.7$) exhibits a weak but clear power dependence, scaling as $n_{e,\text{core}} \propto P_{\text{SOL}}^{0.27 \pm 0.03}$. This result is consistent with L-mode density limit scalings reported on other tokamaks, such as ASDEX Upgrade [8]. In contrast, the separatrix density displays a stronger relationship, scaling as $n_{e,\text{sep}} \propto P_{\text{SOL}}^{0.42 \pm 0.04}$. This relatively strong power dependence is reminiscent of the density limit observed in stellarators, where power balance is known to be the dominant constraint [9, 10].

These disparate power scalings constitute a central finding of this work; they indicate that the density saturation is not governed by a single, global mechanism. Instead, it suggests that

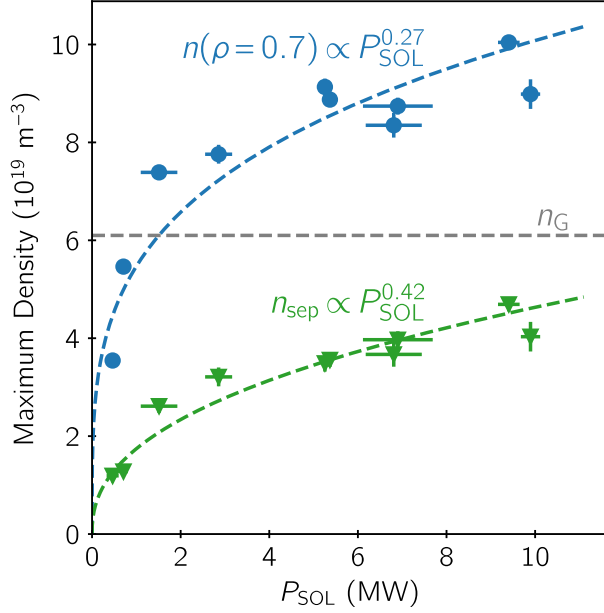


FIG. 3. The maximum density achieved at two different radial positions (core and separatrix) in negative triangularity (NT) discharges as a function of the loss power entering the scrape-off layer (P_{SOL}). The horizontal dashed line indicates the Greenwald density.

distinct physical processes, with different sensitivities to heating power, are responsible for limiting the density in the core and edge regions. This hypothesis—that core saturation is dominated by turbulent transport while edge saturation is governed by radiative instabilities—guides the investigative framework for the remainder of this paper.

B. Profile Evolution and Confinement Degradation Towards Density Limit

1. Reduced Temperature and Rotational Shear at High Density

As the plasma approaches the density limit, its equilibrium profiles evolve in a manner that signals a clear degradation of thermal confinement. This evolution, shown for a representative high-power discharge in Fig. 4, provides important insight into the underlying transport dynamics.

The electron density profile [Fig. 4(a)] rises across the radius but remains notably flat in the core, indicating that strong particle transport persists even at high densities. The degraded con-

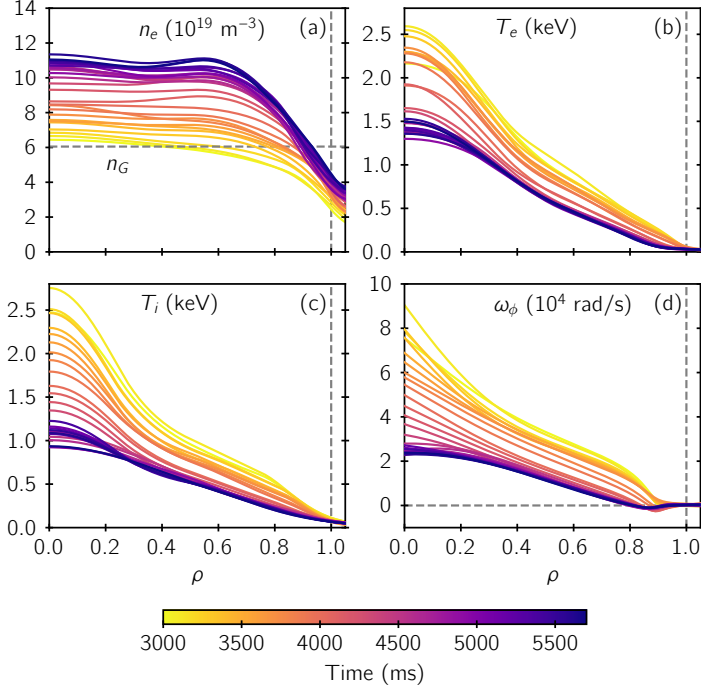


FIG. 4. Temporal evolution of equilibrium profiles in a high-power discharge (shot 194133). (a) Electron density n_e , (b) electron temperature T_e , (c) carbon ion temperature T_i , and (d) toroidal rotation rate ω_ϕ . The profiles are colored according to the time in milliseconds (ms), with earlier times shown in yellow and later times shown in purple. The dashed vertical line indicates the location of the separatrix.

finement is accompanied by a loss of thermal energy, as both the electron and ion temperature profiles collapse [Figs. 4(b), 4(c)]. A noticeable feature is the pronounced flattening of the edge T_e profile, a classic signature of intensified radiative cooling at the plasma boundary.

Another critical change occurs in the plasma rotation. The toroidal rotation profile [Fig. 4(d)], initially peaked in the core, progressively collapses with increasing density. This loss of core rotation directly dismantles the dominant component of the radial electric field (E_r), a key factor for turbulence suppression. As shown in Fig. 5, the core E_r shear, initially strong, diminishes and ultimately vanishes as the density limit is approached.

This cascade of events, from intensified edge cooling to the collapse of core rotation and E_r shear, indicates that the plasma's ability to suppress turbulence deteriorates with rising density. The loss of this stabilizing flow shear enables enhanced turbulent transport that governs the core density limit, as subsequent sections will demonstrate.

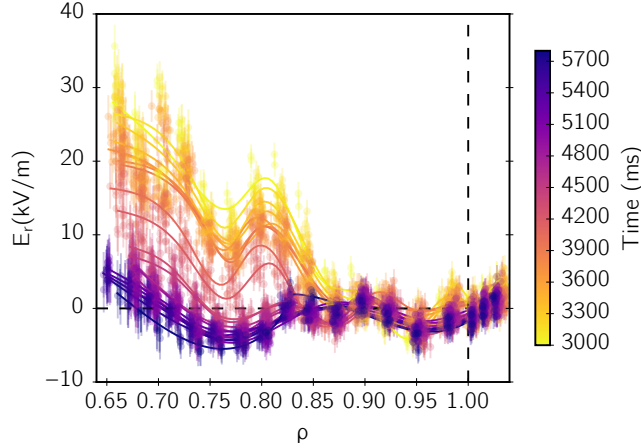


FIG. 5. The temporal evolution of the edge radial electric field (E_r) at the outer mid-plane in a high-power discharge (shot 194133). The profiles are color-coded by time, with earlier times shown in yellow and later times in purple. The vertical dashed lines indicate the approximate location of the separatrix.

2. Divergent Evolution of Turbulence in Different Regions

The degradation of thermal confinement described above coincides with a dramatic divergence in turbulent activity across the plasma, as illustrated in Fig. 6 for a high-power discharge. A critical transition occurs at approximately 3700 ms (vertical dashed line), marking the onset of strong edge cooling. Before this event, the turbulence evolution is relatively uniform; afterward, it diverges sharply between different spatial regions.

Initially, both core and edge densities rise together [Fig. 6(a)], accompanied by a steady increase in the amplitude of local, intermediate- k turbulence at the low-field side (LFS) midplane ($\rho \approx 0.95$), as measured by Doppler backscattering [Fig. 6(d)]. This period of evolution ends abruptly at the 3700 ms transition. Immediately following this transition, the LFS turbulence saturates. This saturation coincides with the clamping of the edge density and the sharp drop in local electron temperature [Fig. 6(b)].

In contrast, turbulence in other regions intensifies. Line-integrated, low- k density fluctuations on the high-field side (HFS), measured by the CO₂ interferometer, grows substantially [Figs. 6(e), 6(f)]. A similar growth is observed in the line-integrated midplane fluctuations measured by the RIP diagnostic [Figs. 6(g), 6(h)].

This divergent evolution—saturation of localized turbulence on the LFS versus continued,

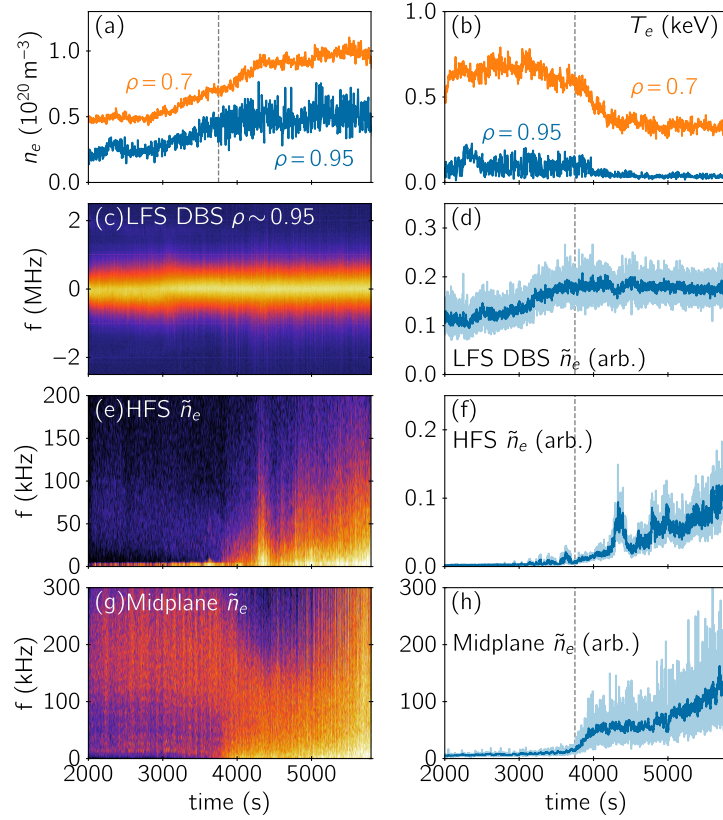


FIG. 6. Time evolution of electron density and temperature and turbulence characteristics during a high-density discharge (shot 194133): (a) Local n_e measured at $\rho = 0.7$ and 0.95 ; (b) Local T_e at $\rho = 0.7$ and 0.95 ; (c) Spectrogram and (d) RMS amplitude of density fluctuations measured by Doppler back-scattering at the low-field side mid-plane ($\rho \approx 0.95$); (e) Spectrogram and (f) RMS amplitude of line-integrated density fluctuations measured by CO_2 interferometer at the high field side; (g) Spectrogram and (h) RMS amplitude of line-integrated density fluctuations measured by RIP along the mid-plane. The vertical dashed line indicates the onset of enhanced turbulence.

strong growth of HFS and core fluctuations—reveals a profound poloidal asymmetry in the transport dynamics. This asymmetry strongly suggests that the density limit is not a globally uniform process but is instead triggered by a localized instability on the high-field side—likely the radiative phenomenon that we investigate next.

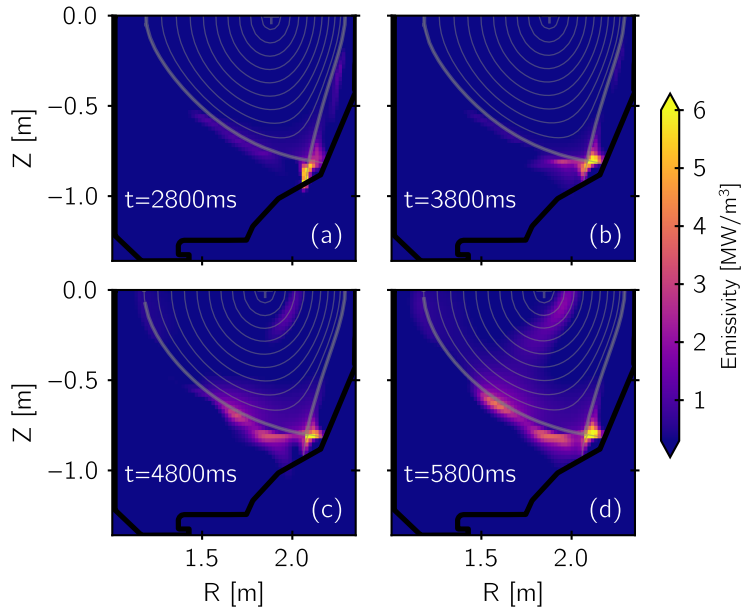


FIG. 7. Temporal evolution of the 2D distribution of radiated power during a representative high-power discharge (shot 194133), reconstructed from bolometer measurements. (a) Before density ramp-up ($t = 2800$ ms), (b) enhanced divertor radiation ($t = 3800$ ms), (c) radiation front leaving inner divertor ($t = 4800$ ms), and (d) radiation front intensified at the HFS ($t = 5800$ ms).

C. The Edge Density Limit: A Radiatively Driven Phenomenon

1. Visualizing the HFS Radiation Front

The poloidally asymmetric turbulence described previously points to a localized radiative instability as the trigger for the edge density limit. Here, we examine the 2D radiated power distribution, reconstructed from bolometer measurements, to visualize the formation and evolution of this instability. Figure 7 presents a time-sequence of this evolution. While geometrically similar to a disruptive MARFE [16, 36], the feature observed here is a quasi-stable, non-disruptive radiation front that is directly linked to the observed density saturation.

The evolution of this front proceeds in clear stages. Early in the discharge ($t = 2800$ ms), before the density ramp, the radiation is concentrated at the inner divertor target, characteristic of a standard attached divertor [Fig. 7(a)]. As plasma density increases ($t = 3800$ ms), an intense radiation zone emerges near the X-point, signaling the birth of the radiative front [Fig. 7(b)]. This event coincides with the onset of the divergent turbulence seen in Fig. 6. With a further

increase in density ($t = 4800$ ms), this front detaches from the divertor and propagates upward along the HFS separatrix [Fig. 7(c)]. This movement is strongly correlated with the localized edge cooling and turbulence saturation. Finally ($t = 5800$ ms), the front moves further inboard and its emissivity intensifies [Fig. 7(d)].

This sequence provides direct visual evidence of a developing radiative instability on the HFS. This dynamic structure appears to be the primary driver of the edge density limit. Notably, the eventual discharge termination was caused by a subsequent drop in NBI power that triggered an $n = 1$ locked mode and was not a direct consequence of the radiation front.

2. Radiative Cooling and the Onset of HFS Turbulence

The formation of the HFS radiation front actively cools the plasma and triggers a dramatic shift in the local turbulent state. Figure 8 provides quantitative evidence of this transition. As the HFS radiated power increases beyond a critical threshold, the edge plasma parameters and HFS turbulence changes fundamentally. The RMS amplitude of the line-integrated HFS density fluctuations (\tilde{n}_{HFS}), measured by the CO₂ interferometer passing through the radiation front, serves as a proxy for the instability's strength.

The effect of edge cooling can be characterized by the dimensionless adiabaticity parameter [37], $\alpha_{\text{adia}} = k_{\parallel}^2 v_{te}^2 / \omega \nu_{ei} \propto \frac{T_e^{5/2}}{n_e}$, which represents the comparison between parallel electron motion and turbulent timescales. Here, k_{\parallel} is the parallel wavenumber of turbulence, v_{te} is the electron thermal velocity, ω is the turbulence frequency, and ν_{ei} is the electron-ion collision frequency. When $\alpha_{\text{adia}} < 1$, the plasma enters a non-adiabatic regime where drift-wave instabilities are expected to grow. As shown in Fig. 8(a), the onset of the strong HFS radiation drives α_{adia} to plummet below 1.

This transition into a non-adiabatic state coincides with a surge in HFS turbulence. Figure 8(b) shows that the RMS amplitude of HFS density fluctuations (\tilde{n}_e) increases sharply as the radiated power crosses the same threshold. The entire event is correlated with a degradation in plasma performance, as indicated by the drop in the H_{98y2} confinement factor (color scale). This finding demonstrates that the HFS radiation front alters the local plasma state, unleashing the turbulence that may ultimately limit the edge density.

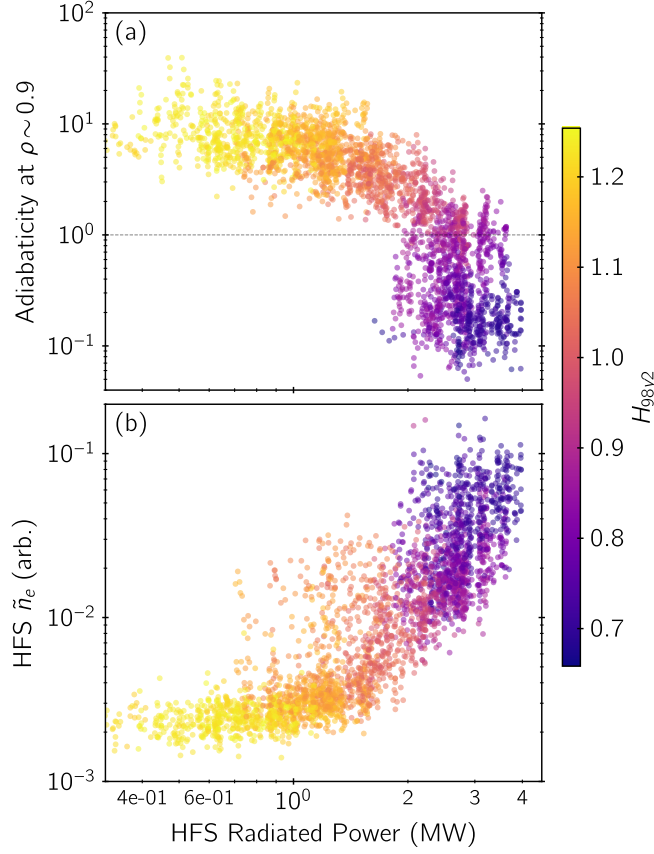


FIG. 8. Transition to a degraded confinement state driven by HFS radiated power. (a) The edge adiabaticity parameter at $\rho \sim 0.9$ drops below unity as radiated power exceeds a critical threshold. (b) This transition coincides with a surge in the RMS amplitude of HFS density fluctuations (\tilde{n}_e). Data points are colored by the H_{98y2} energy confinement factor, showing a clear shift from a high-confinement (yellow) to a low-confinement (purple) state. The plot is in log-log scale. 20 ms moving average is applied to fluctuation data.

3. Clamping of the Edge Density

The preceding evidence indicates that the HFS radiative instability is the cause of the edge density saturation. To test this hypothesis quantitatively, we correlate the local edge density with the instability's strength, again using the RMS amplitude of the line-integrated HFS density fluctuations (\tilde{n}_{HFS}) as a proxy.

Figure 9 plots the edge density (at $\rho = 0.95$) against \tilde{n}_{HFS} on a log-log scale. The data, compiled from multiple discharges, reveals a dramatic bifurcation in the plasma behavior, defined by two distinct operational regimes that are distinguished by the energy confinement

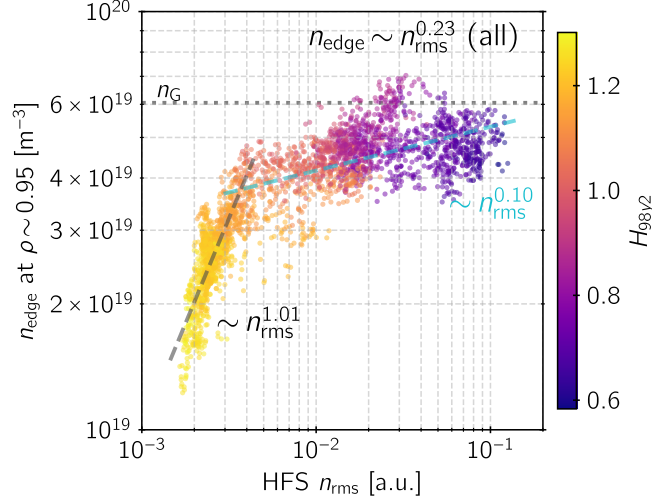


FIG. 9. Edge density at $\rho = 0.95$ is plotted against the RMS amplitude of the density fluctuations measured by the HFS CO₂ interferometer. The power law relationships for low- and high-turbulence regimes are indicated by the gray and cyan lines, respectively. The plot is in log-log scale. The data points are colored according to the energy confinement factor H_{98y2} . The dashed horizontal line represents the Greenwald density.

factor, H_{98y2} .

At low turbulence amplitudes, the plasma is in a high-confinement state (high H_{98y2} , yellow points). In this phase, the edge density and turbulence grow together, following a nearly linear relationship ($n_{e,\text{edge}} \propto \tilde{n}_{\text{HFS}}^{1.0}$). This represents a state where turbulence-driven transport has not yet begun to limit the density.

This linear relationship breaks down abruptly once the turbulence level surpasses a critical threshold, at which point the system transitions to a degraded-confinement state (low H_{98y2} , purple points). While the instability amplitude continues to grow by nearly an order of magnitude, the edge density saturates almost completely, exhibiting a nearly flat scaling ($n_{e,\text{edge}} \propto \tilde{n}_{\text{HFS}}^{0.1}$).

This bifurcation provides strong evidence that the edge density limit is not a gradual process, but a sharp transition triggered by the radiative instability. Once initiated, the instability clamps the edge density at a value consistently below the Greenwald limit, leading to a significant increase in HFS turbulence. The apparent overall relationship across both regimes ($n_{e,\text{edge}} \propto \tilde{n}_{\text{HFS}}^{0.23}$) also masks the sharpness of this critical transition.

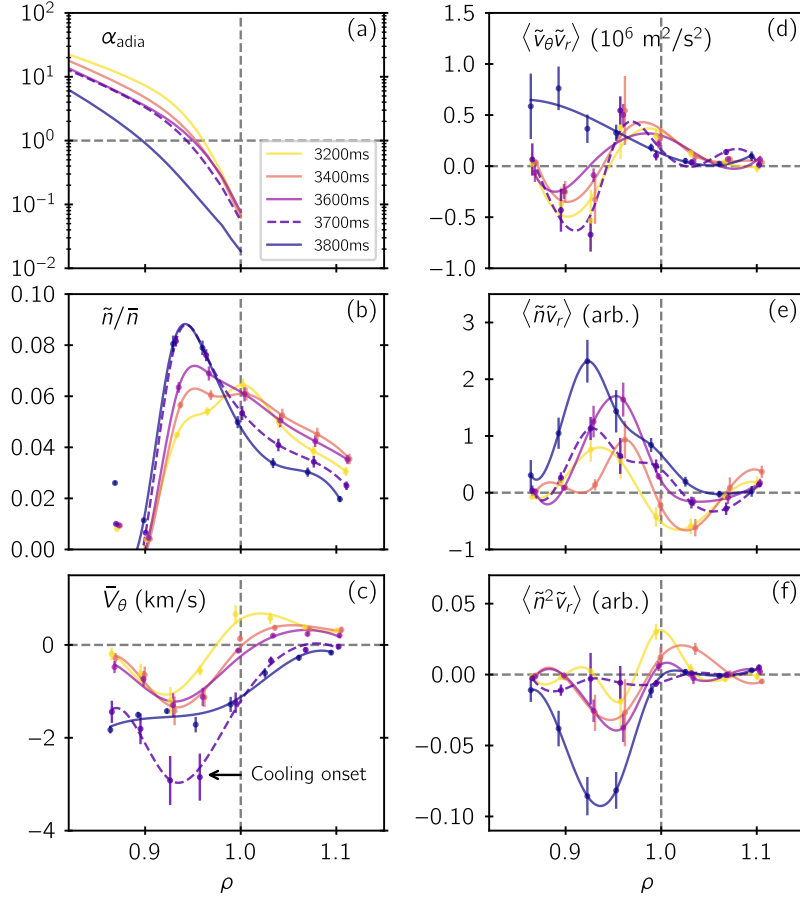


FIG. 10. Radial profiles of LFS edge turbulence characteristics during radiative cooling in a low-power NT discharge (shot 194131): (a) adiabaticity parameter, (b) normalized density fluctuation amplitude, (c) mean poloidal phase velocity, and (d) Reynolds stress $\langle \tilde{v}_\theta \tilde{v}_r \rangle$, (e) particle flux $\langle \tilde{n} \tilde{v}_r \rangle$, and (f) turbulent spreading flux $\langle \tilde{n}^2 \tilde{v}_r \rangle$. The profiles are colored by the time from lighter to darker. Particularly, the profiles corresponding to the onset of the radiative cooling (about 3700 ms) are marked by dashed curves in purple.

4. Breakdown of Zonal Flow Regulation

The onset of the HFS radiative instability has global consequences, leading to a failure of turbulence self-regulation across the plasma edge. We use BES measurements on the low-field side to observe this breakdown in detail (Fig. 10), revealing the microphysical mechanism responsible for enhanced transport.

The trigger for this breakdown is the transition to the non-adiabatic regime. As the edge cools

with the onset of the radiation front ($t \approx 3700$ ms), the dimensionless adiabaticity parameter, α_{adia} , drops below unity [Fig. 10(a)]. This transition is known to fundamentally alter drift-wave turbulence, weakening the mechanisms that generate stabilizing zonal flows [13, 37].

While the fluctuation amplitude on the LFS saturates (as seen in Fig. 6), the underlying dynamics show a flattening of the Reynolds stress profile [$\langle \tilde{v}_\theta \tilde{v}_r \rangle$, Fig. 10(d)]. This collapse of the primary nonlinear drive for zonal flows (i.e., the Reynolds force, $\mathcal{F}_{\text{Re}} = -\partial_r \langle \tilde{v}_\theta \tilde{v}_r \rangle$) signifies a breakdown in the zonal flow regulation mechanism. Concurrently, the mean poloidal phase velocity of turbulence [$\langle \tilde{v}_\theta \rangle$, Fig. 10(c)] also collapses.

This breakdown in zonal flow regulation directly drives particle loss. The outward turbulent particle flux [$\langle \tilde{n} \tilde{v}_r \rangle$, Fig. 10(e)] grows significantly, while the turbulent spreading flux [$\langle \tilde{n}^2 \tilde{v}_r \rangle$, Fig. 10(f)] indicates that turbulence intensity is propagating inward from the separatrix. These measurements suggest a compelling narrative: edge cooling initiates a transition to the non-adiabatic turbulent regime, which disables zonal flow regulation and unleashes enhanced transport.

D. The Core Density Limit: A Transition to Avalanche-like Turbulence

While the edge density saturates below the Greenwald limit, the core density continues to rise, often reaching much higher values than n_G . This decoupling implies that a separate, core-localized mechanism must govern the core density profile. Here, we present evidence that this mechanism is not a simple enhancement of diffusive transport, but a fundamental transition in its character to intermittent, avalanche-like behavior. This transition is enabled by the collapse of the stabilizing $E_r \times B$ shear, as shown previously in Fig. 5.

1. Statistical Signatures of Avalanche-like Transport,

The statistical properties of the core density fluctuations, measured by the RIP diagnostic at the midplane, reveal three distinct signatures of this transition.

First, the probability density function (PDF) of the fluctuation amplitudes evolves from Gaussian to heavy-tailed. Early in the discharge the PDF is Gaussian [yellow in Fig. 11(a)], characteristic of diffusive transport. As the density limit is approached, however, the PDF develops pronounced, non-Gaussian tails [purple in Fig. 11(a)]. This signifies a shift to a

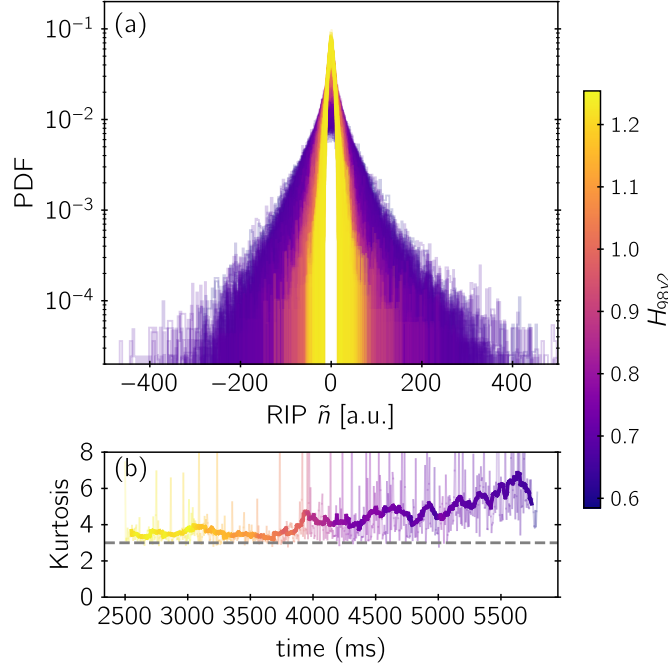


FIG. 11. (a) Time evolution of the probability density function of the amplitudes of line-integrated density fluctuations measured by the RIP system at the midplane. (b) The time history of the kurtosis of the amplitudes of the line-integrated density fluctuations. The horizontal dashed line presents the kurtosis value of a Gaussian distribution.

transport regime dominated by large-amplitude, intermittent events. The growing intermittency is quantified by the kurtosis of the PDF, which rises from the Gaussian value of 3 to about 6 [Fig. 11(b)].

Second, the frequency spectrum of the turbulence develops a $1/f$ -type power-law scaling. As the plasma evolves with rising density, a distinctive power-law scaling emerges at a wide range of frequencies [Fig. 12(a)]. Such a spectrum is a classic signature of self-organized criticality (SOC) and avalanche dynamics, where transport occurs via cascading events spanning a wide range of scales [38–40].

Third, the transport acquires long-range temporal correlations, quantified by the Hurst exponent (H), a measure of the persistence in a time series [Fig. 12(b)]. The Hurst exponent rises from $H \approx 0.5$, the value for uncorrelated, random-walk events (diffusive transport), to $H \approx 0.8$ as the density limit is approached. A value of $H > 0.5$ indicates persistent, correlated dynamics, another key feature of avalanche-like transport. This rise in H is strongly correlated with a substantial decrease in the energy confinement factor H_{98y2} , linking the emergence of

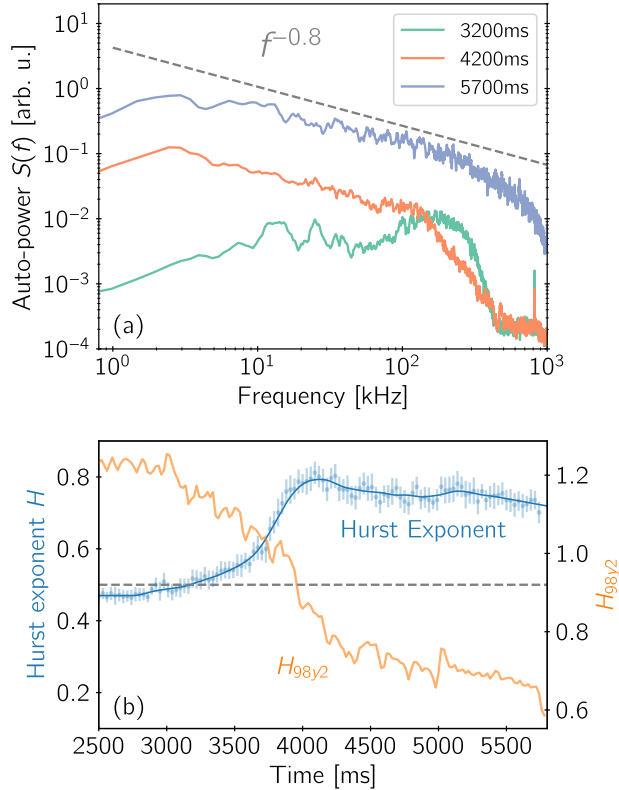


FIG. 12. (a) Auto-power spectrum of the line-integrated midplane density fluctuations measured by RIP at different times. The dashed line indicates the power-law spectrum of $1/f^{0.8}$. (b) Time evolution of the Hurst exponent calculated from the RIP data (blue) and energy confinement factor (orange). The horizontal dashed line indicates a Hurst exponent of 0.5, corresponding to a random walk process.

this non-diffusive transport regime to the degradation in plasma performance.

Collectively, these three independent signatures—heavy-tailed PDFs, a $1/f$ power spectrum, and an elevated Hurst exponent—provide a consistent and compelling picture: core transport undergoes a fundamental transition from a diffusive to an intermittent, avalanche-like regime, which may be the mechanism for the core density limit.

2. Core Density Saturation by Avalanche-like Turbulence

The emergence of avalanche-like dynamics provides a clear hypothesis for the core density limit: the large, intermittent transport events ultimately clamps the density profile. We test this hypothesis by correlating the core density (at $\rho \approx 0.7$) with the RMS amplitude of the midplane

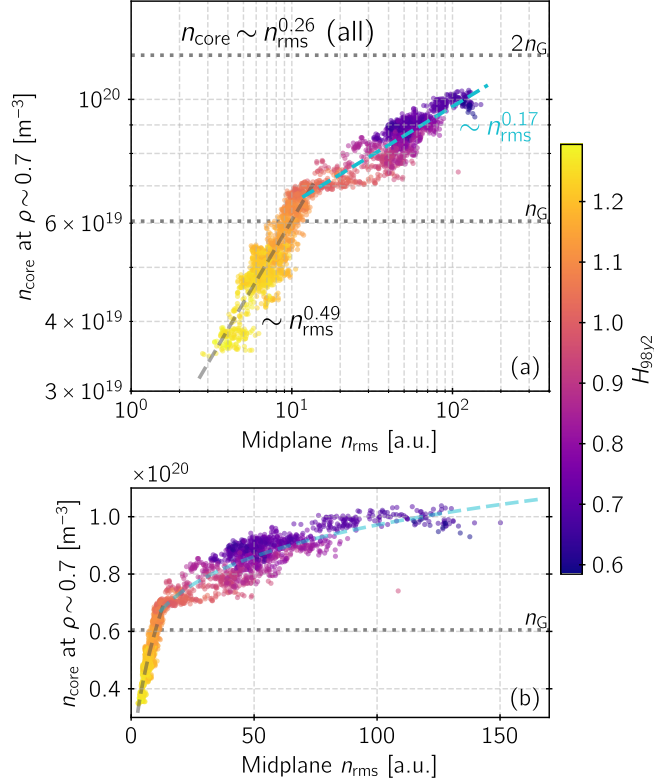


FIG. 13. Core density at $\rho = 0.7$ is plotted against the RMS amplitude of the density fluctuations measured by the midplane RIP interferometers on a log-log scale (a) and linear scale (b). The data points are colored according to the normalized total radiation. The dotted horizontal line represents the Greenwald density. Power law relationships for low- and high-turbulence regimes are indicated by the gray and cyan lines, respectively.

turbulence measured by RIP.

As shown in Fig. 13, data compiled from multiple discharges reveal a clear bifurcation between two transport regimes, distinguished by their confinement properties (H_{98y2}).

In the low-turbulence, high-confinement regime ($H_{98y2} > 1.0$, yellow points), which corresponds to the diffusive state, the core density rises robustly with increasing turbulence amplitude, following a strong power-law scaling of $n_{e,\text{core}} \propto \tilde{n}_{\text{rms}}^{0.49}$. This phase represents a state where fueling remains effective despite the presence of turbulence.

This behavior changes dramatically as the transport transitions to the high-turbulence, low-confinement regime ($H_{98y2} < 1.0$, purple points), which corresponds to the avalanche-like state. Here, the scaling weakens significantly, flattening to $n_{e,\text{core}} \propto \tilde{n}_{\text{rms}}^{0.17}$. This transition to a

much weaker scaling demonstrates that the core fueling has become highly inefficient. The avalanche-like fluctuations effectively prevent any significant increases in density, leading to a saturation of the core density profile. This saturation occurs at densities far exceeding the Greenwald limit, approaching $2n_G$.

The weak overall scaling of density with turbulence ($n_{\text{core}} \propto \tilde{n}_{\text{rms}}^{0.26}$) is consistent with the weak macroscopic power scaling of the core density limit ($n_{e,\text{core}} \propto P_{\text{SOL}}^{0.27 \pm 0.03}$) found previously. This alignment confirms that the core density limit is governed not by simple power balance, but by a fundamental transition in the turbulent transport itself, from diffusive to avalanche-like, which saturates the density profile.

IV. CONCLUSION AND DISCUSSION

This study re-examined the underlying physics of the density limit using negative triangularity plasmas on the DIII-D tokamak. Our findings reveal that the density limit, at least in NT plasmas without an H-mode edge, is not a singular disruptive boundary, but a multifaceted saturation phenomenon governed by distinct physical mechanisms: an edge density limit triggered by a radiative instability, and a core density limit driven by avalanche-like turbulent transport. Moreover, this study demonstrate sustained, non-disruptive operations at densities up to 1.8 times the Greenwald limit with substantial auxiliary heating.

At the plasma edge, the density limit manifests as an abrupt saturation event triggered by a radiative instability on the high-field side. While geometrically similar to a disruptive MARFE, this radiative instability acts as a quasi-stable front that clamps the edge density at a level below the Greenwald limit, without terminating the discharge.

In contrast, the core density is not directly constrained by the edge cooling and continues to rise well beyond the Greenwald limit. Its saturation is instead governed by a fundamental shift in the nature of core turbulence. As the density increases, core transport transitions from a diffusive state to one characterized by intermittent, avalanche-like dynamics. This is supported by signatures including heavy-tailed PDFs, $1/f$ -type power spectra, and elevated Hurst exponents. This persistent, non-diffusive transport regime prevents further increases in the core density.

The dual mechanisms of regional density saturation are consistent with the disparate power scalings observed for the core ($n_{e,\text{core}} \propto P_{\text{SOL}}^{0.27}$) and edge ($n_{e,\text{edge}} \propto P_{\text{SOL}}^{0.42}$). The power-dependent

nature of this limit and its link to transport physics show a compelling resemblance to density limits observed in stellarators. This suggests a potentially universal physics of power balance and transport that transcends specific magnetic configurations, pointing to a more fundamental basis for the density limit in magnetically confined plasmas.

These findings also present a potential strategy for achieving high Greenwald fraction operation in future tokamaks, particularly those utilizing negative triangularity configurations. Success hinges on addressing the distinct physical mechanisms governing the density limit in the core and edge. The edge radiative instability can be mitigated through advanced divertor designs and impurity control aimed at managing boundary heat fluxes. Concurrently, advanced techniques to suppress core turbulence, such as strong rotational shear flows and Shafranov shift, can be developed to optimize density profiles and confinement. By pursuing these parallel control strategies, the operational space of future reactors can be extended into stable, high-density regimes well beyond conventional scaling.

ACKNOWLEDGMENTS

The authors gratefully acknowledge the invaluable support and contributions of the entire DIII-D team in performing this experiment. This material is based upon work supported by the U.S. Department of Energy, Office of Science, Office of Fusion Energy Sciences, using the DIII-D National Fusion Facility, a DOE Office of Science user facility, under Awards Nos. DE-FC02-04ER54698, DE-SC0019352, DE-SC0019004, DE-FG02-97ER54415, DE-AC52-07NA27344, and DE-SC0016154. The author (P.H.D.) acknowledges support from LLNL-led SciDAC ABOUND Project SCW1832. The author (O.S.) performed this work within the framework of the EUROfusion Consortium, via the Euratom Research and Training Programme (Grant Agreement No. 101052200– EUROfusion) and funded by the Swiss State Secretariat for Education, Research and Innovation (SERI). Views and opinions expressed are however those of the author(s) only and do not necessarily reflect those of the European Union, the European Commission, or SERI. Neither the European Union nor the European Commission nor SERI can be held responsible for them.

Disclaimer: This report was prepared as an account of work sponsored by an agency of the United States Government. Neither the United States Government nor any agency thereof, nor any of their employees, makes any warranty, express or implied, or assumes any legal

liability or responsibility for the accuracy, completeness, or usefulness of any information, apparatus, product, or process disclosed, or represents that its use would not infringe privately owned rights. Reference herein to any specific commercial product, process, or service by trade name, trademark, manufacturer, or otherwise does not necessarily constitute or imply its endorsement, recommendation, or favoring by the United States Government or any agency thereof. The views and opinions of authors expressed herein do not necessarily state or reflect those of the United States Government or any agency thereof.

- [1] J. D. Lawson, Some Criteria for a Power Producing Thermonuclear Reactor, [Proceedings of the Physical Society. Section B](#) **70**, 6 (1957).
- [2] M. Greenwald, J. Terry, S. Wolfe, S. Ejima, M. Bell, S. Kaye, and G. Neilson, A new look at density limits in tokamaks, [Nuclear Fusion](#) **28**, 2199 (1988).
- [3] M. Greenwald, Density limits in toroidal plasmas, [Plasma Physics and Controlled Fusion](#) **44**, R27 (2002).
- [4] T. Petrie, A. Kellman, and M. Mahdavi, Plasma density limits during Ohmic L mode and ELMing H mode operation in DIII-D, [Nuclear Fusion](#) **33**, 929 (1993).
- [5] M. Giacomini, A. Pau, P. Ricci, O. Sauter, T. Eich, the ASDEX Upgrade team, JET Contributors, and the TCV team, First-Principles Density Limit Scaling in Tokamaks Based on Edge Turbulent Transport and Implications for ITER, [Physical Review Letters](#) **128**, 185003 (2022).
- [6] R. Singh and P. H. Diamond, Zonal shear layer collapse and the power scaling of the density limit: Old L-H wine in new bottles, [Plasma Physics and Controlled Fusion](#) **64**, 084004 (2022).
- [7] P. Zanca, F. Sattin, D. Escande, and JET Contributors, A power-balance model of the density limit in fusion plasmas: Application to the L-mode tokamak, [Nuclear Fusion](#) **59**, 126011 (2019).
- [8] P. Manz, T. Eich, and O. Grover, The power dependence of the maximum achievable H-mode and (disruptive) L-mode separatrix density in ASDEX Upgrade, [Nuclear Fusion](#) **63**, 076026 (2023).
- [9] S. Sudo, Y. Takeiri, H. Zushi, F. Sano, K. Itoh, K. Kondo, and A. Iiyoshi, Scalings of energy confinement and density limit in stellarator/heliotron devices, [Nuclear Fusion](#) **30**, 11 (1990).
- [10] J. Miyazawa, R. Sakamoto, S. Masuzaki, B. Peterson, N. Tamura, M. Goto, I. Yamada, K. Narihara, K. Tanaka, T. Tokuzawa, M. Shoji, M. Kobayashi, H. Arimoto, K. Kondo, S. Murakami, H. Funaba, S. Sakakibara, M. Osakabe, S. Morita, Y. Nagayama, N. Ohyabu, H. Yamada, A. Komori, and

- O. Motojima, Density limit study focusing on the edge plasma parameters in LHD, [Nuclear Fusion](#) **48**, 015003 (2008).
- [11] B. N. Rogers, J. F. Drake, and A. Zeiler, Phase Space of Tokamak Edge Turbulence, the L Transition, and the Formation of the Edge Pedestal, [Physical Review Letters](#) **81**, 4396 (1998).
- [12] B. LaBombard, J. Hughes, D. Mossessian, M. Greenwald, B. Lipschultz, J. Terry, and T. A. C.-M. Team, Evidence for electromagnetic fluid drift turbulence controlling the edge plasma state in the Alcator C-Mod tokamak, [Nuclear Fusion](#) **45**, 1658 (2005).
- [13] R. Hong, G. Tynan, P. Diamond, L. Nie, D. Guo, T. Long, R. Ke, Y. Wu, B. Yuan, M. Xu, and The HL-2A Team, Edge shear flows and particle transport near the density limit of the HL-2A tokamak, [Nuclear Fusion](#) **58**, 016041 (2018).
- [14] T. Long, P. Diamond, R. Ke, L. Nie, M. Xu, X. Zhang, B. Li, Z. Chen, X. Xu, Z. Wang, T. Wu, W. Tian, J. Yuan, B. Yuan, S. Gong, C. Xiao, J. Gao, Z. Hao, N. Wang, Z. Chen, Z. Yang, L. Gao, Y. Ding, Y. Pan, W. Chen, G. Hao, J. Li, W. Zhong, and X. Duan, Enhanced particle transport events approaching the density limit of the J-TEXT tokamak, [Nuclear Fusion](#) **61**, 126066 (2021).
- [15] M. Z. Tokar, Synergy of Anomalous Transport and Radiation in the Density Limit, [Physical Review Letters](#) **91**, 095001 (2003).
- [16] B. Lipschultz, B. LaBombard, E. Marmor, M. Pickrell, J. Terry, R. Watterson, and S. Wolfe, Marfe: An edge plasma phenomenon, [Nuclear Fusion](#) **24**, 977 (1984).
- [17] W. Suttrop, K. Buchl, J. Fuchs, M. Kaufmann, K. Lackner, M. Maraschek, V. Mertens, R. Neu, M. Schittenhelm, M. Sokoll, and H. Zohm, Tearing mode formation and radiative edge cooling prior to density limit disruptions in ASDEX upgrade, [Nuclear Fusion](#) **37**, 119 (1997).
- [18] D. A. Gates and L. Delgado-Aparicio, Origin of Tokamak Density Limit Scalings, [Physical Review Letters](#) **108**, 165004 (2012).
- [19] M. Kikuchi, T. Takizuka, S. Medvedev, T. Ando, D. Chen, J. Li, M. Austin, O. Sauter, L. Villard, A. Merle, M. Fontana, Y. Kishimoto, and K. Imadera, L-mode-edge negative triangularity tokamak reactor, [Nuclear Fusion](#) **59**, 056017 (2019).
- [20] K. E. Thome, M. E. Austin, A. Hyatt, A. Marinoni, A. O. Nelson, C. Paz-Soldan, F. Scotti, W. Boyes, L. Casali, C. Chrystal, S. Ding, X. D. Du, D. Eldon, D. Ernst, R. Hong, G. R. McKee, S. Mordijck, O. Sauter, L. Schmitz, J. L. Barr, M. G. Burke, S. Coda, T. B. Cote, M. E. Fenstermacher, A. Garofalo, F. O. Khabanov, G. J. Kramer, C. J. Lasnier, N. C. Logan, P. Lunia, A. G. McLean, M. Okabayashi,

- D. Shiraki, S. Stewart, Y. Takemura, D. D. Truong, T. Osborne, M. A. Van Zeeland, B. S. Victor, H. Q. Wang, J. G. Watkins, W. P. Wehner, A. S. Welander, T. M. Wilks, J. Yang, G. Yu, L. Zeng, and the DIII-D Team, Overview of results from the 2023 DIII-D negative triangularity campaign, [Plasma Physics and Controlled Fusion](#) **66**, 105018 (2024).
- [21] M. E. Austin, A. Marinoni, M. L. Walker, M. W. Brookman, J. S. deGrassie, A. W. Hyatt, G. R. McKee, C. C. Petty, T. L. Rhodes, S. P. Smith, C. Sung, K. E. Thome, and A. D. Turnbull, Achievement of Reactor-Relevant Performance in Negative Triangularity Shape in the DIII-D Tokamak, [Physical Review Letters](#) **122**, 115001 (2019).
- [22] A. Marinoni, M. Austin, A. Hyatt, S. Saarelma, F. Scotti, Z. Yan, C. Chrystal, S. Coda, F. Glass, J. Hanson, A. McLean, D. Pace, C. Paz-Soldan, C. Petty, M. Porkolab, L. Schmitz, F. Sciortino, S. Smith, K. Thome, F. Turco, and The Diii-D Team, Diverted negative triangularity plasmas on DIII-D: The benefit of high confinement without the liability of an edge pedestal, [Nuclear Fusion](#) **61**, 116010 (2021).
- [23] A. O. Nelson, L. Schmitz, C. Paz-Soldan, K. E. Thome, T. B. Cote, N. Leuthold, F. Scotti, M. E. Austin, A. Hyatt, and T. Osborne, Robust Avoidance of Edge-Localized Modes alongside Gradient Formation in the Negative Triangularity Tokamak Edge, [Physical Review Letters](#) **131**, 195101 (2023).
- [24] S. Coda, A. Merle, O. Sauter, L. Porte, F. Bagnato, J. Boedo, T. Bolzonella, O. Février, B. Labit, A. Marinoni, A. Pau, L. Pigatto, U. Sheikh, C. Tsui, M. Vallar, and T. Vu, Enhanced confinement in diverted negative-triangularity L-mode plasmas in TCV, [Plasma Physics and Controlled Fusion](#) **64**, 014004 (2022).
- [25] J. Luxon, A design retrospective of the DIII-D tokamak, [Nuclear Fusion](#) **42**, 614 (2002).
- [26] O. Sauter, R. Hong, A. Marinoni, F. Scotti, P. H. Diamond, C. Paz-Soldan, D. Shiraki, K. E. Thome, M. A. Van Zeeland, H. Q. Wang, Z. Yan, and the negD-DIII-D Team, Operation above the Greenwald density limit in high performance DIII-D negative triangularity discharges, [Plasma Physics and Controlled Fusion](#) **67**, 075009 (2025).
- [27] T. N. Carlstrom, F. Glass, D. Du, A. G. McLean, D. Taussig, and R. Boivin, Thomson scattering measurements on DIII-D using in-vessel laser mirrors and lenses to diagnose a new divertor location, [Review of Scientific Instruments](#) **89**, 10C111 (2018).
- [28] C. Chrystal, K. H. Burrell, B. A. Grierson, S. R. Haskey, R. J. Groebner, D. H. Kaplan, and A. Briesemeister, Improved edge charge exchange recombination spectroscopy in DIII-D, [Review of Scien-](#)

- tific Instruments **87**, 11E512 (2016).
- [29] A. W. Leonard, W. H. Meyer, B. Geer, D. M. Behne, and D. N. Hill, 2D tomography with bolometry in DIII-Da), *Review of Scientific Instruments* **66**, 1201 (1995).
- [30] M. A. Van Zeeland, R. L. Boivin, T. N. Carlstrom, T. Deterly, and D. K. Finkenthal, Fiber optic two-color vibration compensated interferometer for plasma density measurements, *Review of Scientific Instruments* **77**, 10F325 (2006).
- [31] J. Chen, W. X. Ding, D. L. Brower, D. Finkenthal, and R. Boivin, A Faraday-effect polarimeter for fast magnetic dynamics measurement on DIII-D, *Review of Scientific Instruments* **89**, 10B101 (2018).
- [32] G. R. McKee, R. J. Fonck, D. K. Gupta, D. J. Schlossberg, M. W. Shafer, and R. L. Boivin, High sensitivity beam emission spectroscopy for core plasma turbulence imaging (invited), *Review of Scientific Instruments* **77**, 10F104 (2006).
- [33] W. A. Peebles, T. L. Rhodes, J. C. Hillesheim, L. Zeng, and C. Wannberg, A novel, multichannel, comb-frequency Doppler backscatter system, *Review of Scientific Instruments* **81**, 10D902 (2010).
- [34] J. Damba, Q. Pratt, V. H. Hall-Chen, R. Hong, R. Lantsov, R. Ellis, and T. L. Rhodes, Evaluation of a new DIII-D Doppler backscattering system for higher wavenumber measurement and signal enhancement, *Review of Scientific Instruments* **93**, 103549 (2022).
- [35] AP. Smirnov, RW. Harvey, and K. Kupfer, A general ray tracing code GENRAY, *Bull Amer. Phys. Soc* **39**, 1626 (1994).
- [36] B. Lipschultz, Review of MARFE phenomena in tokamaks, *Journal of Nuclear Materials* **145–147**, 15 (1987).
- [37] M. Wakatani and A. Hasegawa, A collisional drift wave description of plasma edge turbulence, *The Physics of Fluids* **27**, 611 (1984).
- [38] T. S. Hahm and P. H. Diamond, Mesoscopic Transport Events and the Breakdown of Fick’s Law for Turbulent Fluxes, *Journal of the Korean Physical Society* **73**, 747 (2018).
- [39] P. A. Politzer, Observation of Avalanchelike Phenomena in a Magnetically Confined Plasma, *Physical Review Letters* **84**, 1192 (2000).
- [40] P. H. Diamond and T. S. Hahm, On the dynamics of turbulent transport near marginal stability, *Physics of Plasmas* **2**, 3640 (1995).